Energy Materials

Supplementary Materials

Synergistic iron-oxygen coordination in spent lithium iron phosphate slag for nitrate electroreduction to ammonia

Tianyu Wang[1,2], Yu Qing[1], Deyou Liu[1], Meiying Wei[1], Keqin Dai[3], Hongjie Guo[2,*], Hongliang Li[1,*]

[1]College of Mining Engineering, Taiyuan University of Technology, Taiyuan 030024, Shanxi, China.
[2]National Laboratory of Solid State Microstructures, School of Sustainable Energy and Resources, Jiangsu Key Laboratory of Artificial Functional Materials, Collaborative Innovation Center of Advanced Microstructures, Frontiers Science Center for Critical Earth Material Cycling, Nanjing University, Nanjing 215004, Jiangsu, China.
[3]School of International Education, Wuhan University of Technology, Wuhan 430070, Hubei, China.

Correspondence to: Dr. Hongjie Guo, National Laboratory of Solid State Microstructures, School of Sustainable Energy and Resources, Jiangsu Key Laboratory of Artificial Functional Materials, Collaborative Innovation Center of Advanced Microstructures, Frontiers Science Center for Critical Earth Material Cycling, Nanjing University, Nanjing 215004, Jiangsu, China. E-mail: 602025840006@smail.nju.edu.cn; Prof. Hongliang Li, College of Mining Engineering, Taiyuan University of Technology, Taiyuan 030024, Shanxi, China. lihongliang222@126.com

Characterizations

X-ray diffraction (XRD) analyses were performed on a Bruker D8 ADVANCE X-ray diffractometer with Cu Kα radiation at 40 kV and 40 mA. Scanning electron microscopy (SEM) analyses were conducted using a Hitachi S4800 microscope. Transmission electron microscopy (TEM), high-resolution TEM (HRTEM) and energy-dispersive X-ray spectroscopy (EDS) were performed on a FEI TECNAI G2 F20 microscope. X-ray photoelectron spectroscopy (XPS) analyses were carried out

on a Thermo Scientific ESCALAB 250Xi unit equipped with an Al-Kα X-ray excitation source. Electron paramagnetic resonance (EPR) spectra were recorded on a Bruker EMXplus 10/12 unit equipped with an Oxford ESR910 liquid helium cryostat. Raman and *in-situ* Raman spectra were recorded on a Horiba LabRAM HR Evolution Raman microscope with a 532 nm laser excitation source. Liquid products were analyzed using a Bruker AVANCE NEO 600 MHz ^{1}H NMR spectrometer. Electrochemical measurements were conducted using a CHI 1140D electrochemical workstation (Shanghai Chenhua Instrument Co., Ltd., China).

^{15}N isotope-labeling experiment and ^{1}H NMR analysis

^{15}N isotope-labeling experiments were performed to identify the nitrogen source of the synthesized ammonia. The standard catholyte was replaced by 1 M KOH + 0.1 M K$^{15}NO_3$ (98 atom% ^{15}N), and electrolysis was carried out at -0.4 V vs. RHE under otherwise identical conditions. After electrolysis, the catholyte was collected, diluted if necessary, and adjusted to pH ~2 with 0.1 M HCl to ensure complete conversion of dissolved NH_3 into NH_4^+.

For ^{1}H NMR analysis, 0.5 mL of the acidified sample was mixed with 50 μL D_2O as the deuterium lock solvent. Maleic acid was added as a reference standard. The sample was then analyzed on a Bruker AVANCE NEO 600 MHz spectrometer. As a control, the same procedure was performed using $^{14}NO_3^-$-containing electrolyte. The product obtained from the $^{15}NO_3^-$ electrolyte showed the characteristic doublet of $^{15}NH_4^+$, while that from the $^{14}NO_3^-$ electrolyte showed the triplet of $^{14}NH_4^+$, confirming that the detected ammonia was generated from nitrate electroreduction rather than environmental contamination.

EPR measurements

EPR measurements were performed to monitor hydrogen-related radical species generated at the catalyst/electrolyte interface during electrolysis. The electrolyte used for EPR measurements was 1 M KOH in the absence or presence of 0.1 M KNO_3. DMPO (5,5-dimethyl-1-pyrroline N-oxide) was used as the spin-trapping agent.

In a typical measurement, chronoamperometry was first carried out at the selected potential for 5 min in an electrolyte containing DMPO. Immediately after electrolysis,

an aliquot of the electrolyte near the working electrode was collected and transferred into a quartz capillary/EPR tube for spectral acquisition. The EPR spectra were recorded on a Bruker EMX-plus 10/12 spectrometer at room temperature.

The same procedure was performed in nitrate-free and nitrate-containing electrolytes under otherwise identical conditions. The intensity change of the DMPO-trapped hydrogen-related signal was used to evaluate the consumption of reactive hydrogen species during nitrate reduction.

***In-situ* FTIR measurements**

In-situ Fourier transform infrared (FTIR) spectroscopy was performed using a commercial spectrometer equipped with a custom-made spectro-electrochemical cell for *in-situ* electrochemical measurement. The catalyst-coated carbon paper served as the working electrode, a Ti plate was used as the counter electrode, and an Ag/AgCl electrode was used as the reference electrode. The electrolyte was 1 M KOH containing 0.1 M KNO_3 unless otherwise specified. *In-situ* FTIR spectra were collected under open-circuit potential (OCP) and a series of applied potentials during electrolysis. The measured potentials covered OCP, -0.2, -0.3, -0.4, -0.5, and -0.6 V vs. OCP. Before spectrum acquisition at each potential, the electrode was held at the set potential for several minutes to stabilize the electrode interfacial structure.

Construction of Electrocatalytic Ammonia Synthesis System

(1) Electrode Preparation

The working electrode was fabricated as follows: 1 mg of electrocatalyst powder, 950 μL of isopropanol, and 50 μL of Nafion solution (5 wt%, solvent: isopropanol) were mixed and subjected to ultrasonic dispersion for 30 min to form a homogeneous slurry. Subsequently, the slurry was uniformly drop-cast onto the surface of a 1×1 cm^2 hydrophobic microporous carbon paper (AvCarb GDS2120) substrate using a 100 μL micropipette, achieving a precisely controlled catalyst loading of ≈1 $mg \cdot cm^{-2}$.

(2) Electrochemical Setup

A customized 30 mL H-type electrolytic cell and flow cell system from Gaoss Union (Tianjin) Optoelectronic Technology Co., Ltd and Wuhan Zhisheng New Energy Co., Ltd. was employed in this experiment. The anodic and cathodic chambers were

physically separated by a Nafion 117 proton exchange membrane (thickness: 183 μm, density: 360 g·m^{-2}, conductivity: 0.083 S/cm), and the interface between the two chambers was fixed with polytetrafluoroethylene (PTFE) clamps to ensure airtightness of the system and stability of the proton transport pathway during electrolysis. The anolyte was 0.5 mol·L^{-1} Na_2SO_4 solution, and the catholyte was simulated high-concentration nitrate industrial wastewater (1 mol·L^{-1} KOH + 0.1 mol·L^{-1} KNO_3 + 0.1 M KCl, and 0.1 M K_2SO_4). A three-electrode system was adopted: the working electrode was placed in the cathodic chamber (for sample testing), the counter electrode was a IrO2@Ti anode (1×1 cm^2), and an Ag/AgCl electrode was used as the reference electrode in the cathodic chamber. All potential data were reported versus the reversible hydrogen electrode (RHE), converted according to the following equation:

$$E\ (\text{vs. RHE}) = E\ (\text{vs. Ag/AgCl}) + 0.059 \times \text{pH} + 0.197$$

Calculation of Li recovery efficiency

The Li removal/recovery efficiency was calculated as:

$$\text{Li recovery efficiency} = \frac{= n_{Li,S-LFP} - n_{Li,HS-LFP}}{n_{Li,S-LFP}} \times 100\%$$

Density Functional Theory calculation

Spin-polarized DFT calculations were performed using the VASP code with the PAW-PBE method. A plane-wave cutoff energy of 400 eV was adopted, with energy and force convergence thresholds of 10^{-5} eV and 0.02 eV Å^{-1}. A 3 × 3 × 1 k-point mesh was used for Brillouin zone sampling.

Two models were built: crystalline $FePO_4$ and FeO_4/FeO_6/$FePO_4$, to simulate the coordination environment in HS-LFP. Adsorption energy, free energy profile (CHE model), charge density difference, Bader charge, and PDOS were calculated to elucidate the catalytic mechanism. The rate-determining step of NO_3^-RR was identified by comparing the free energy barriers of the two models.

Economic Feasibility Analysis

A preliminary direct-cost estimation was conducted to assess the preparation cost of the HS-LFP catalyst from S-LFP battery black mass. The purpose of this analysis is to illustrate the low direct preparation cost potential of HS-LFP rather than to provide a full gate-to-gate or plant-level techno-economic model. Accordingly, the analysis was intended only as a theoretical lower-bound and sensitivity-based estimate, rather than a strictly equivalent comparison with representative Fe-N-C/MOF and Fe-N-C/SAC catalysts. Therefore, only the direct consumptions associated with catalyst preparation were considered, including raw materials and electricity, while labor, equipment depreciation, plant overhead, wastewater treatment, gas purification, transportation, and profit margins were excluded.

The preparation route of HS-LFP is relatively simple and involves two main steps: (i) mechanical dismantling/pretreatment combined with thermal activation to obtain S-LFP, and (ii) short-time acid leaching to extract Li and reconstruct the Fe-P-O framework into HS-LFP. In the present estimation, the spent LFP feedstock was treated as a near-zero-cost precursor because it originates from retired batteries and is generally regarded as a low-value recycling residue after collection and primary separation. This assumption is reasonable for a gate-fee or waste-derived scenario, in which the Fe- and P-containing fraction after battery recycling has negligible market value compared with intentionally synthesized catalyst precursors.

For the thermal activation step, the energy input was estimated based on heating the recovered cathode powder at 350 °C for 2 h. Considering the relatively small solid mass, batch heating, and the fact that the electricity consumption can be distributed over a large treatment quantity under scaled operation, the effective electricity demand attributable to 1 g of HS-LFP was assumed to be in the range of 0.03-0.08 kWh g^{-1}. Using an industrial electricity price in the U.S. of approximately 0.086 USD kWh^{-1} in 2025, with early 2026 monthly industrial values remaining in a similar range, the corresponding electricity cost is on the order of 0.003-0.007 USD g^{-1}. U.S. Energy Information Administration, Electric Power Monthly, Table 5.6.A. Average Price of Electricity to Ultimate Customers by End-Use Sector, by State. The average U.S. industrial electricity price was approximately 8.50-8.53 cents/kWh in 2025.

The acid-leaching step used 2 M HCl for 10 min. Based on the laboratory solid-to-liquid ratio and the short leaching duration, the direct HCl consumption per gram of final catalyst is low after accounting for solution utilization efficiency and potential recycling of the leaching liquor in scaled operation. In a simplified estimate, the acid consumption was taken to contribute approximately 0.001-0.003 USD g^{-1}. IMARC Group. Hydrochloric Acid Pricing Report, Trend, Index and Forecast Data Report 2025 Edition. Hydrochloric acid settled at USD 151/MT in Germany during Q2 2025. Deionized water and ethanol were used for washing, but their effective contribution was considered minor in a rough direct-cost analysis because the washing step is short, the total amount used per unit catalyst mass is limited, and solvent/water reuse is feasible in practical processing. Accordingly, the raw-material contribution of HS-LFP was estimated to remain below 0.003 USD g^{-1}.

Combining the electricity cost and the direct raw-material cost, the overall direct preparation cost of HS-LFP was estimated to be approximately 0.01 USD g^{-1}, which is presented in Figure 5D as the “direct preparation cost only” scenario. This value should be interpreted as a theoretical lower bound under simplified laboratory-to-scaled assumptions, rather than as a full production or recycling cost. Although this estimate is lower than literature-reported values for representative Fe-N-C/MOF and Fe-N-C/SAC catalysts, such a comparison is not strictly apples-to-apples because the accounting boundaries differ. The large cost advantage mainly originates from three aspects: (i) the use of waste-derived spent LFP as the precursor instead of purpose-designed organic ligands, metal salts, or sacrificial templates; (ii) the absence of complicated multistep precursor synthesis and high-cost nanostructure engineering; and (iii) the mild and short-duration acid reconstruction process, which minimizes reagent consumption[1-3].

It should be emphasized that this estimation reflects the intrinsic low-cost potential of the HS-LFP preparation route rather than a complete plant-level manufacturing cost. In particular, the present analysis does not include battery collection and sorting, large-scale disassembly infrastructure, liquid waste neutralization, environmental compliance, labor, or capital expenditure. Therefore, the resulting value is not directly comparable to literature catalyst costs reported under different system boundaries. To partially address this limitation, we further considered a simplified adjusted scenario

by including the costs of waste neutralization and minimum manual handling, as well as the effect of different acid-leaching liquor recycling efficiencies. Under these more conservative assumptions, the estimated cost increases above the direct-preparation lower bound, but the key qualitative conclusion remains that HS-LFP benefits from a strong feedstock-cost advantage due to the near-zero raw material cost of spent LFP-derived slag. Therefore, the present rough cost analysis is used to support the qualitative economic attractiveness of the waste-derived feedstock route, rather than to claim rigorous quantitative cost superiority over benchmark catalysts.

To provide a more conservative estimate, a simplified sensitivity analysis was performed by considering two additional factors that were excluded from the direct preparation cost: (i) waste neutralization reagent consumption and (ii) minimum manual handling/labor input. In addition, the effect of acid-leaching liquor recycling efficiency was qualitatively examined. Under the direct preparation assumption, the cost is estimated to be approximately 0.01 USD g^{-1}. When a simplified neutralization cost is included, the cost is expected to increase to approximately 0.02 USD g^{-1}. When both neutralization and minimum manual handling are considered, the cost further rises to approximately 0.03-0.05 USD g^{-1}, depending on the assumed liquor recycling efficiency. If the recycling efficiency of the acid-leaching liquor decreases, reagent consumption correspondingly increases, leading to a moderate increase in the adjusted cost estimate. These values are not intended to represent a complete techno-economic assessment, but rather to illustrate that the absolute cost of HS-LFP is sensitive to process-boundary assumptions. Even so, the analysis still indicates that the most important economic advantage of HS-LFP lies in the near-zero raw material cost of the spent-LFP-derived precursor, rather than in a rigorously quantified full-process cost advantage.

Evaluation of Ammonia Synthesis Performance

To systematically evaluate the electrocatalytic nitrate reduction performance of the lithium-extracted residue-based electrodes, multi-angle electrochemical characterization methods were adopted in this chapter. Chronoamperometry (I-t tests) was used to investigate the current response characteristics at different potentials (-0.2 to -0.6 V vs. reversible hydrogen electrode (RHE)) and screen the optimal reaction potential. Linear sweep voltammetry (LSV) was employed to determine the onset potential and polarization behavior of the reaction, combined with the electrochemical

active surface area (ECSA) to quantify the density of active sites on the electrode surface. Electrochemical impedance spectroscopy (EIS) was utilized to analyze the kinetic limitations of charge transfer and mass transfer processes. Potentiostatic cycling tests lasting up to 55 hours were conducted to verify the long-term stability of the electrode, and the ammonia concentration in the catholyte was periodically monitored by UV-Vis spectrophotometry to comprehensively evaluate the Faradaic efficiency, ammonia yield, and long-term stability of the catalyst. The above methodological system provides a systematic research framework for revealing the structure-activity relationship and process compatibility of lithium-extracted residue-based electrodes in electrocatalytic nitrate reduction to ammonia.

The specific performance evaluation formulas for electrocatalytic nitrate reduction to ammonia are as follows:

(1) Ammonia yield (Yield (NH_3))

$$\text{Yield } (NH_3)=\frac{C_{NH_3}\times V}{M_{NH_3}\times t\times m}$$

(2) Faradaic efficiency (FE (NH_3))

$$\text{FE } (NH_3)=\frac{8\times F\times C_{NH_3}\times V}{17\times Q}\times 100\%$$

(3) Nitrate conversion rate (NO_3^- conversion rate)

$$NO_3^- \text{ Conversion rate}=\frac{\Delta C_{NO_3^-}}{C_0}\times 100\%$$

(4) Product selectivity (NO_2^- and NH_4^+ selectivity)

$$NO_2^- \text{ Selectivity } (S_{NO_2^-}) = \frac{\Delta C_{NO_2^-}}{\Delta C_{NO_3^-}} \times 100\%$$

$$NH_4^+ \text{ Selectivity } (S_{NH_4^+}) = \frac{\Delta C_{NH_4^+}}{\Delta C_{NO_3^-}} \times 100\%$$

Where:

C_{NH_3} is the concentration of ammonia in the solution; $\Delta C_{NO_2^-}$ refers to the change in nitrite ion (NO_2^-) concentration before and after electrolysis; $\Delta C_{NO_3^-}$ refers to the change in nitrate ion (NO_3^-) concentration before and after electrolysis; $\Delta C_{NH_4^+}$ refers to the change in ammonium ion (NH_4^+) concentration before and after electrolysis; C_0 is the initial concentration of NO_3^-; V is the volume of the electrolyte; t is the electrolysis time; m is the catalyst loading; F is the Faraday constant, with a value of 96485.17 C mol^{-1}; Q is the total charge passed during the chronoamperometry test.

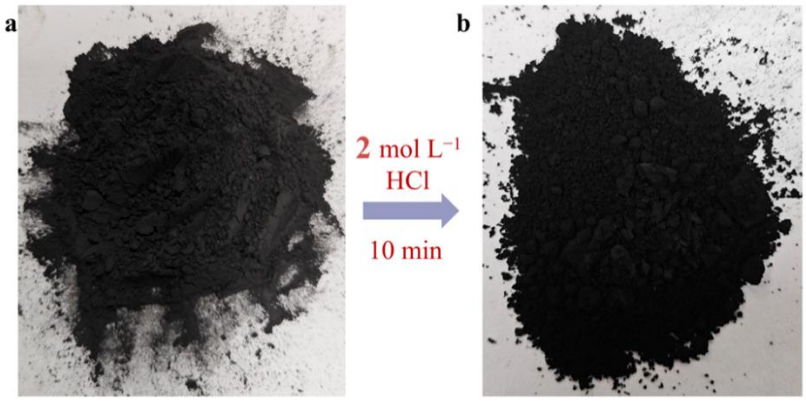

Supplementary Figure 1. (a) Photograph of real S-LFP; (b) Photograph of Li extraction residues (HS-LFP).

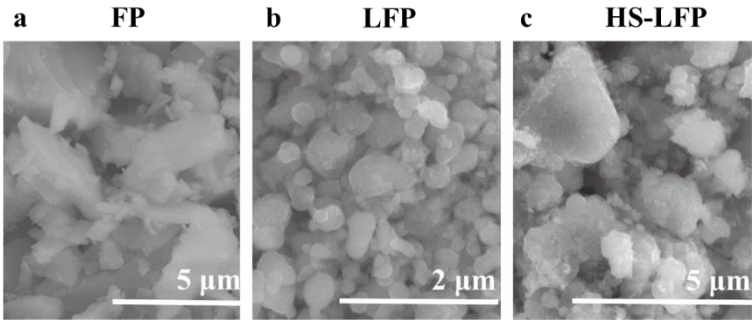

Supplementary Figure 2. SEM images of the morphology of electrodes (a) FP; (b) LFP and (c) HS-LFP.

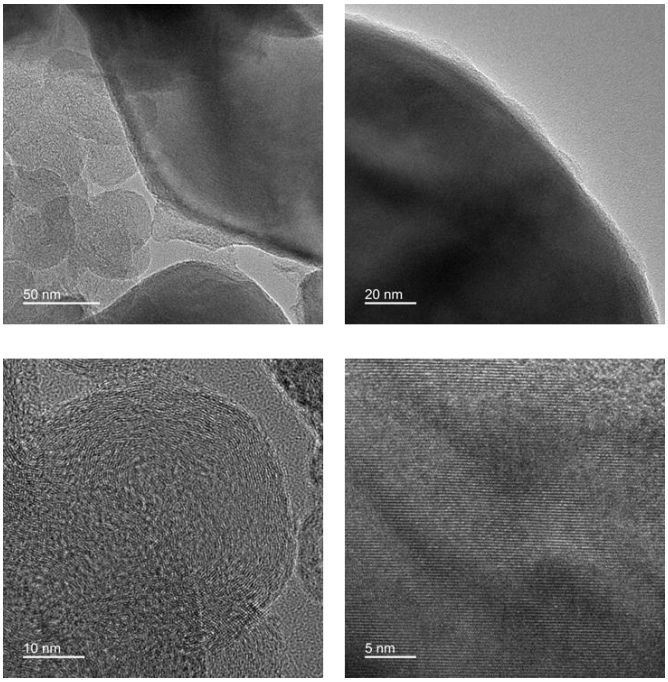

Supplementary Figure 3. TEM image of S-LFP.

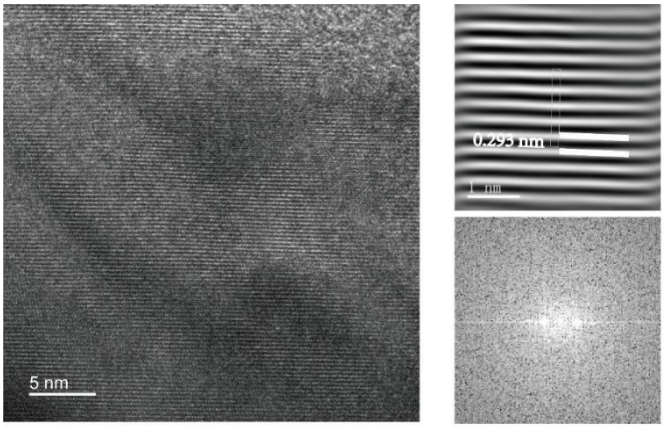

Supplementary Figure 4. HRTEM of S-LFP.

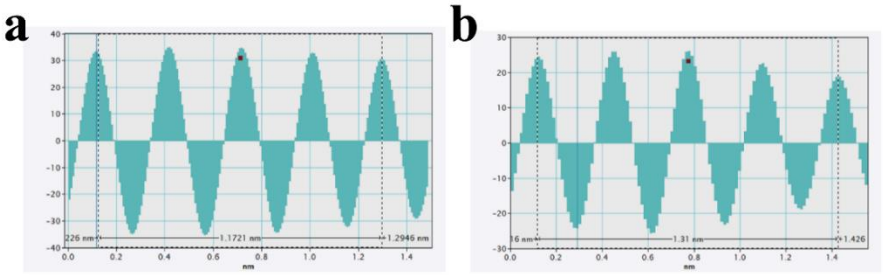

Supplementary Figure 5. FFT analysis of S-LFP (a) and HS-LFP (b).

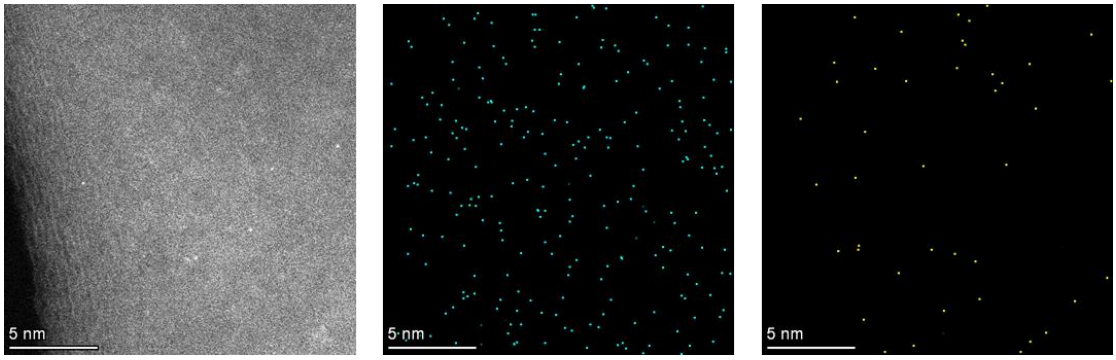

Supplementary Figure 6. Atomic-level structural characterization of Fe sites in HS-LFP. HAADF-STEM image, showing uniformly distributed isolated bright spots corresponding to isolated Fe-O species. Corresponding elemental mapping of O (middle) and Fe (right), respectively, confirming the homogeneous dispersion of Fe species and their co-localization with O in the reconstructed matrix.

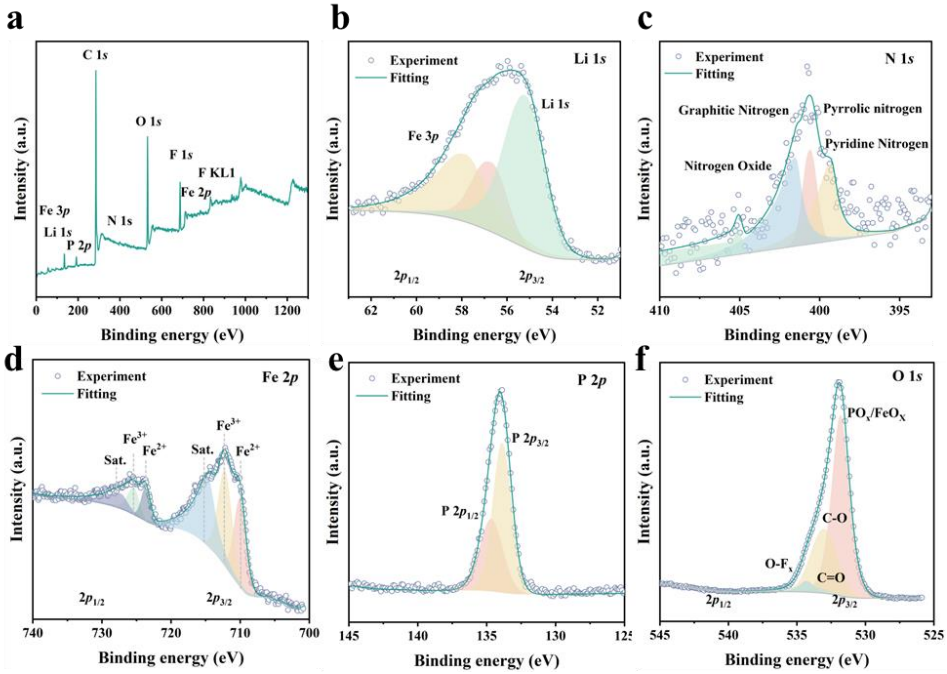

Supplementary Figure 7. XPS analysis of S-LFP.

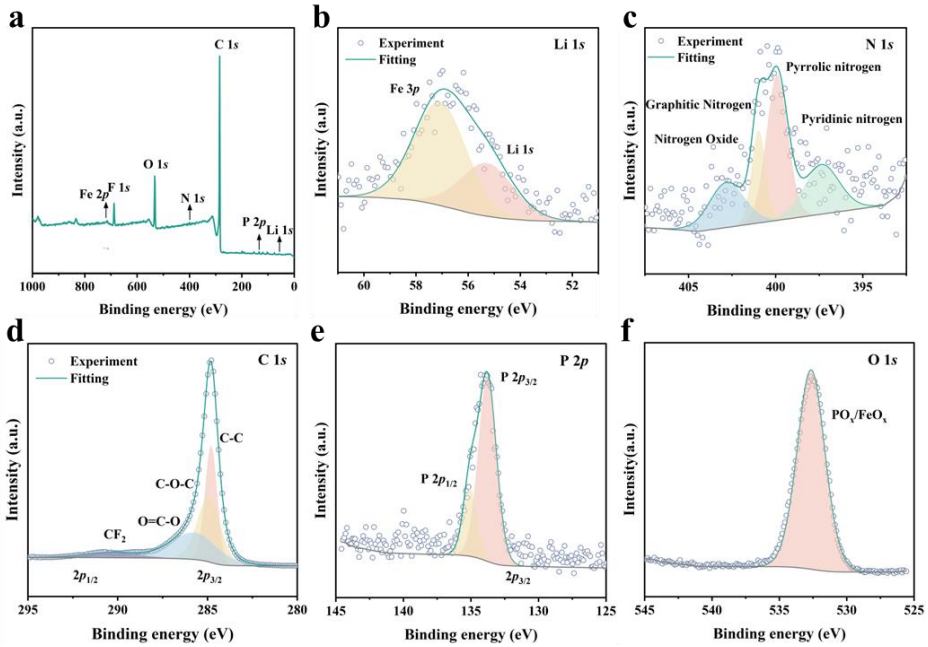

Supplementary Figure 8. XPS analysis of HS-LFP.

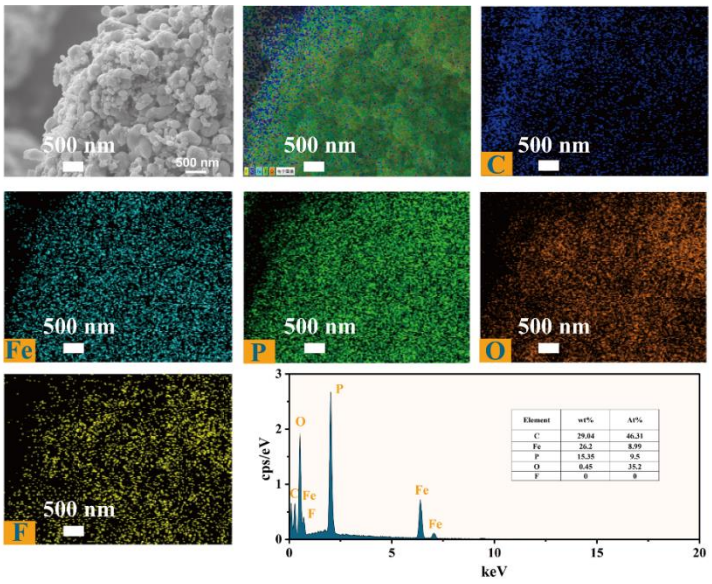

Supplementary Figure 9. EDS mapping of the S-LFP powder.

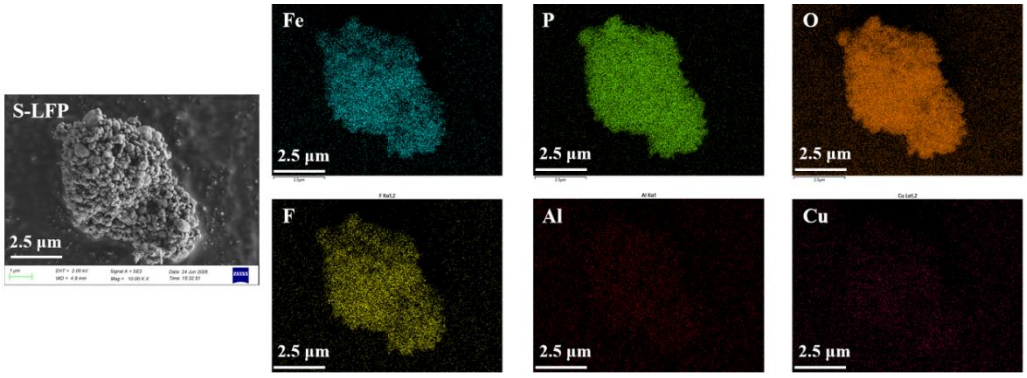

Supplementary Figure 10. EDS mapping of the S-LFP powder (especially Al and Cu).

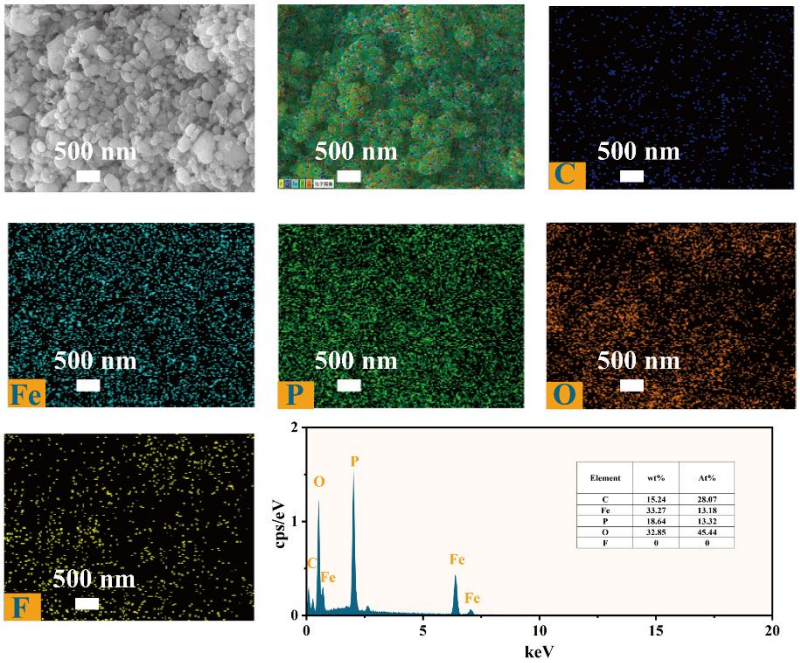

Supplementary Figure 11. EDS mapping of the HS-LFP powder.

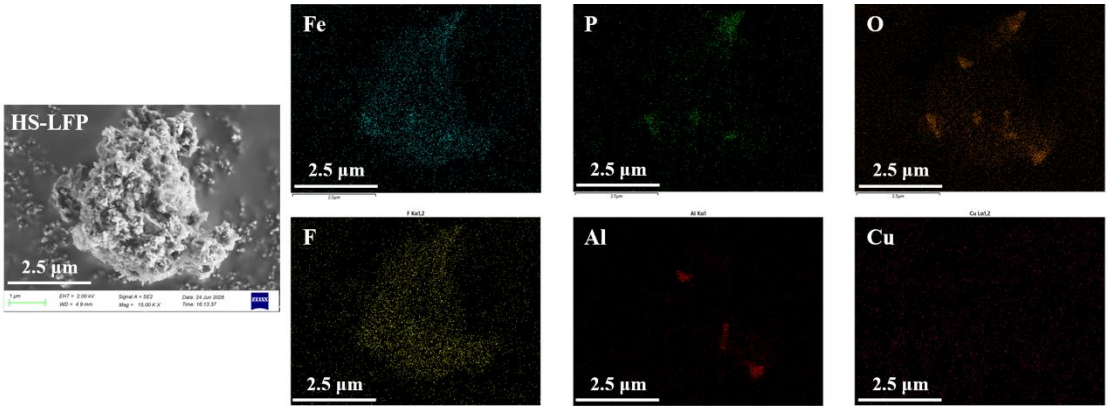

Supplementary Figure 12. EDS mapping of the HS-LFP powder (especially Al and Cu).

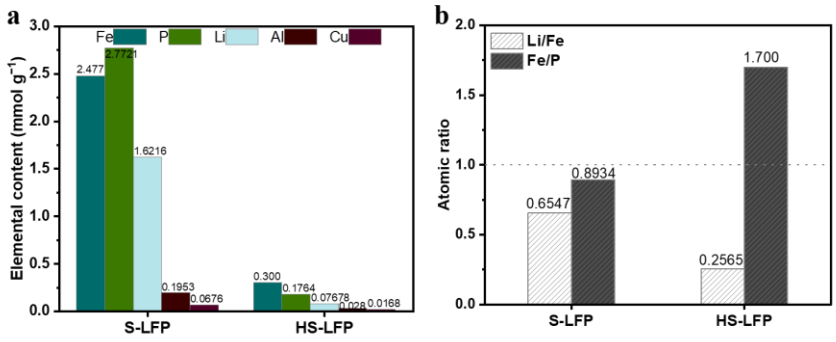

Supplementary Figure 13. ICP results of S-LFP and HS-LFP.

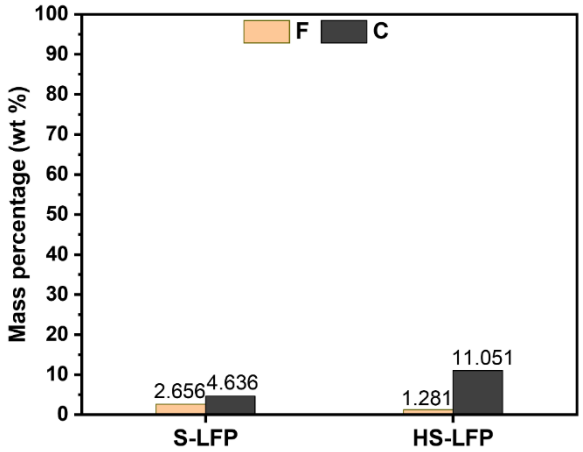

Supplementary Figure 14. Mass percentage of F and C in S-LFP and HS-LFP.

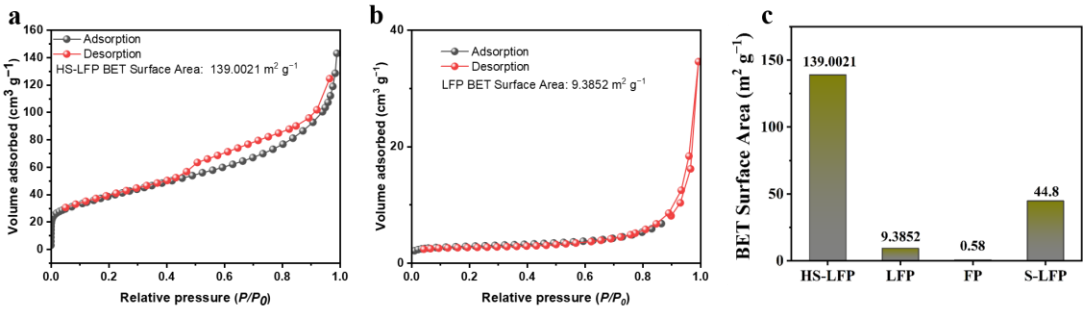

Supplementary Figure 15. N_2 adsorption-desorption isotherms of HS-LFP (a) and LFP (b), and (c) comparison of the BET surface areas of HS-LFP, LFP, FP, and S-LFP.

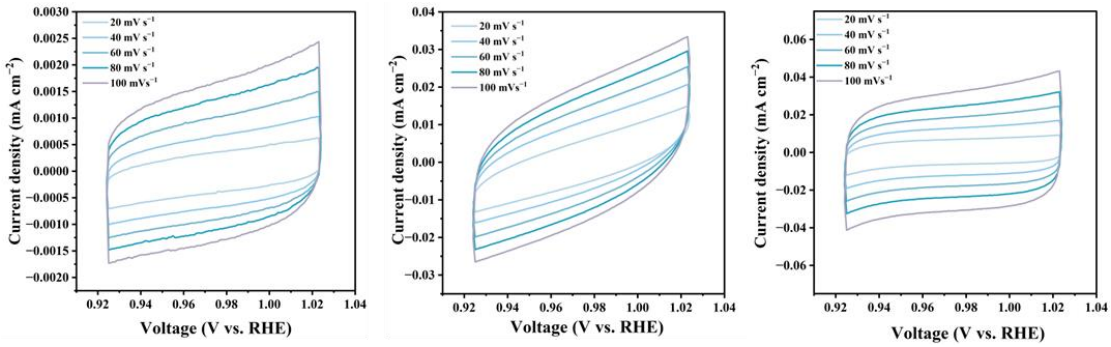

Supplementary Figure 16. CV curves of FP (left), LFP (middle), and HS-LFP (right) at scan rates from 20 to 100 mV s^{-1}, measured for ECSA estimation.

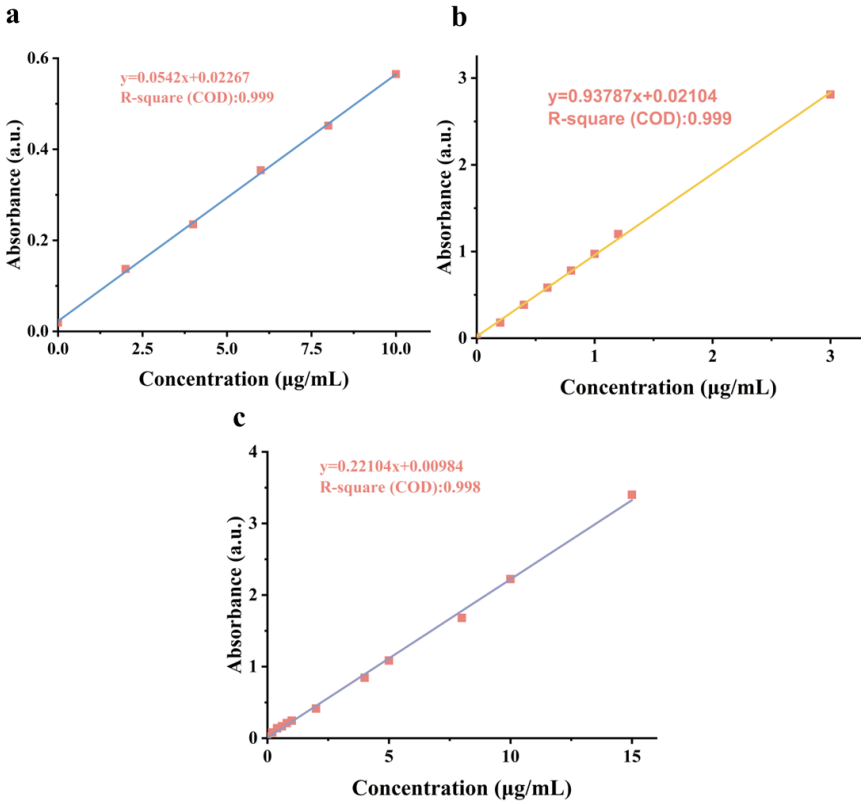

Supplementary Figure 17. Calibration curves for quantitative determination of nitrogen species. (a) NO_3^-, (b) NO_2^-, and (c) NH_4^+. The absorbance-concentration linear relationships and corresponding fitting equations are presented, with R^2 values exceeding 0.998.

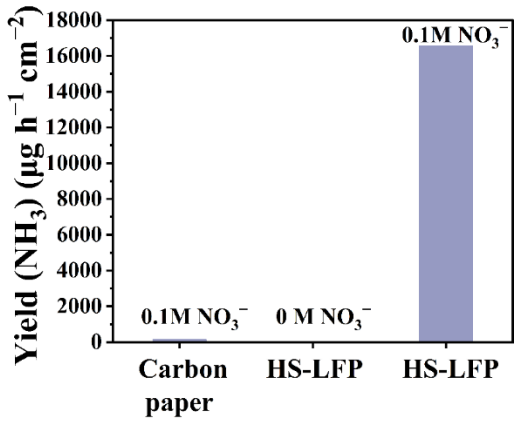

Supplementary Figure 18. Detection of ammonia sources; Carbon paper, HS-LFP (without NO_3^-), HS-LFP (with NO_3^-).

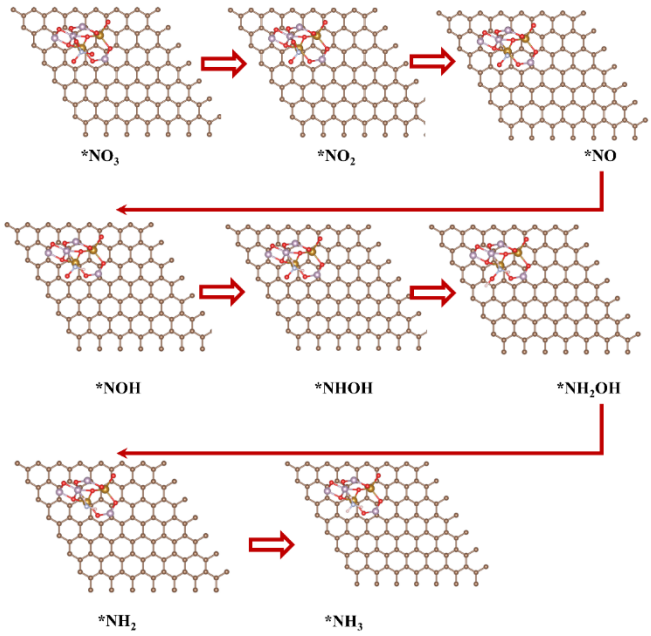

Supplementary Figure 19. Multistep pathway involving *NO_3, *NO_2, *NO, *NOH, *NHOH, *NH_2OH, *NH_2, and *NH_3 intermediates before the final NH_3 release of $FePO_4$ model.

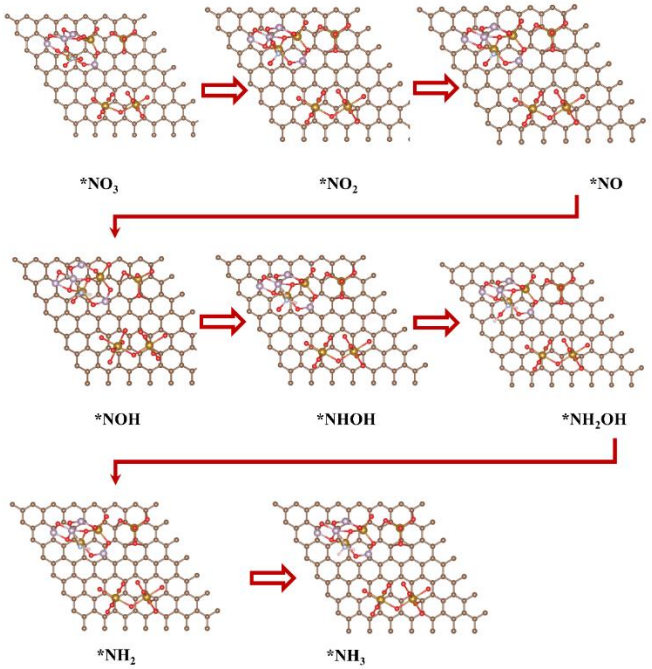

Supplementary Figure 20. Multistep pathway involving $*NO_3$, $*NO_2$, *NO, *NOH, *NHOH, $*NH_2OH$, $*NH_2$, and $*NH_3$ intermediates before the final NH_3 release of $FeO_4/FeO_6/FePO_4$ model.

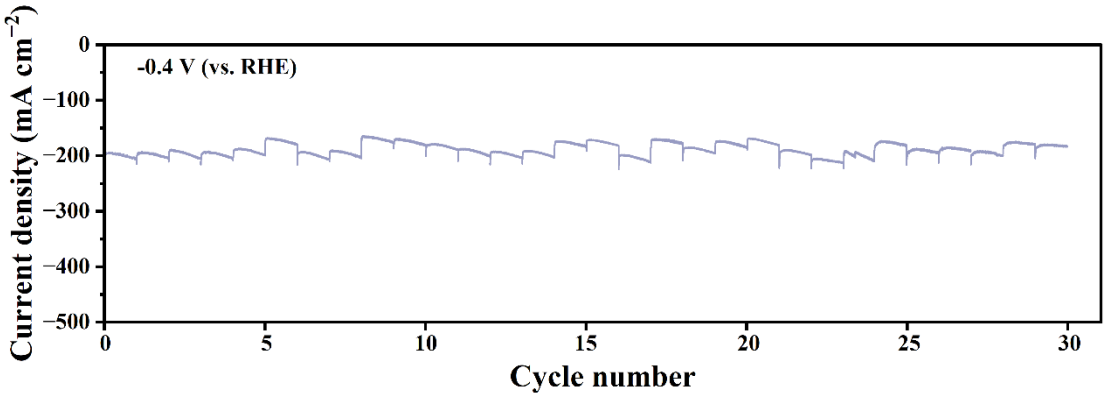

Supplementary Figure 21. The current density of HS-LFP catalyst in the long-term stability test under flow-cell operation.

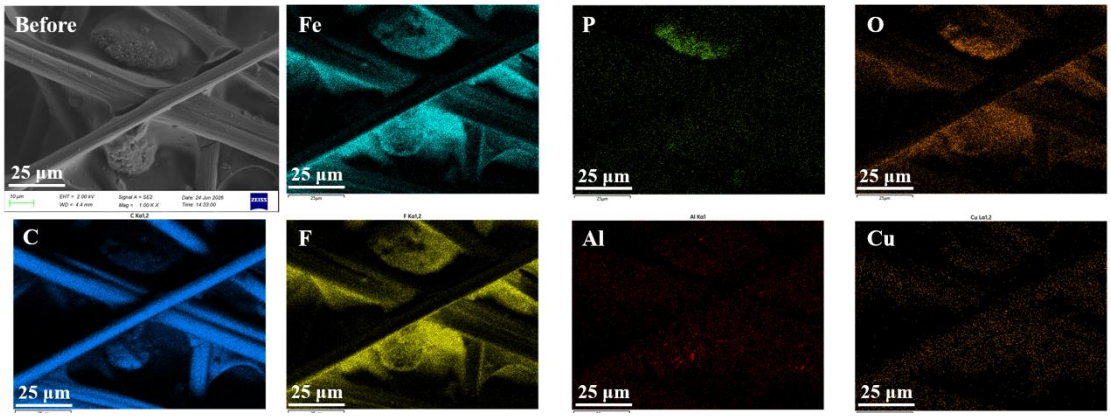

Supplementary Figure 22. EDS mapping of HS-LFP before long-term stability test.

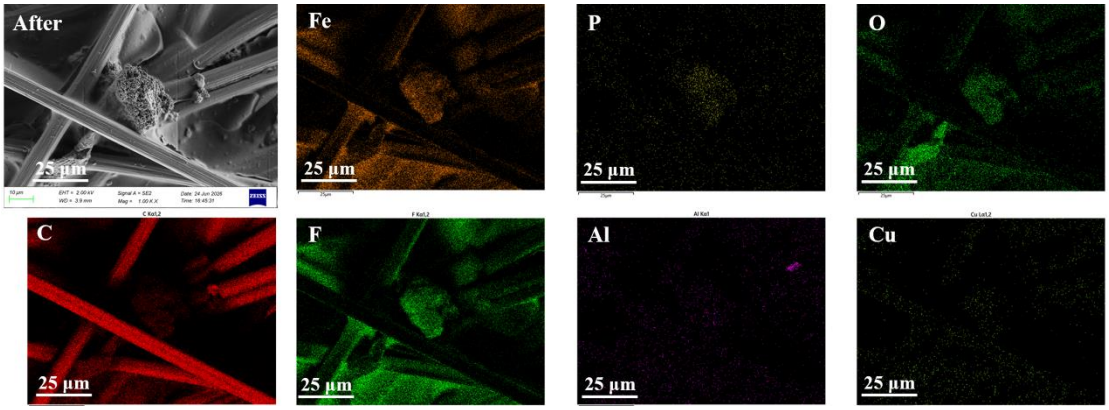

Supplementary Figure 23. EDS mapping of HS-LFP after long-term stability test.

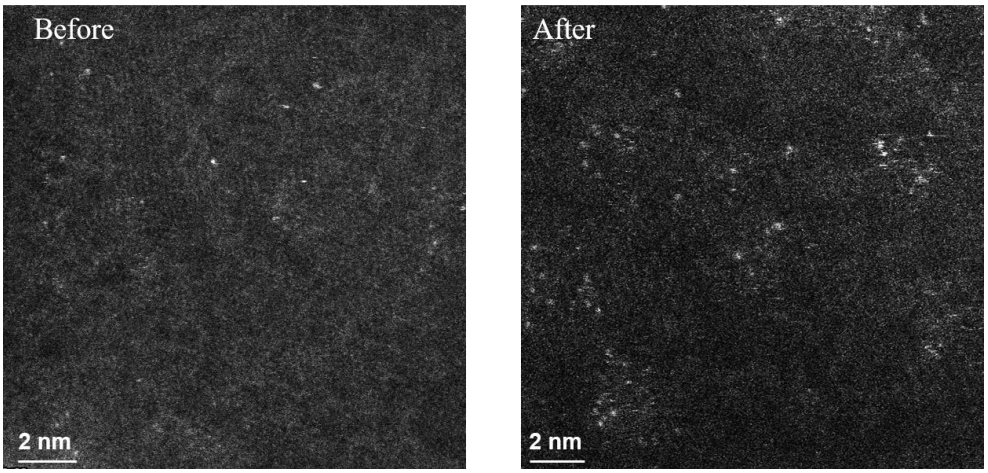

Supplementary Figure 24. HAADF-STEM images of HS-LFP before and after long-term NO_3^-RR electrolysis.

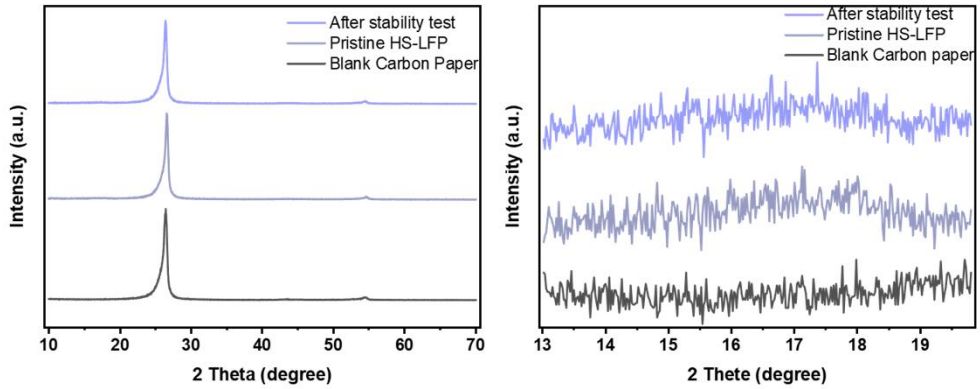

Supplementary Figure 25. XRD patterns of HS-LFP electrode before and after long-term stability test.

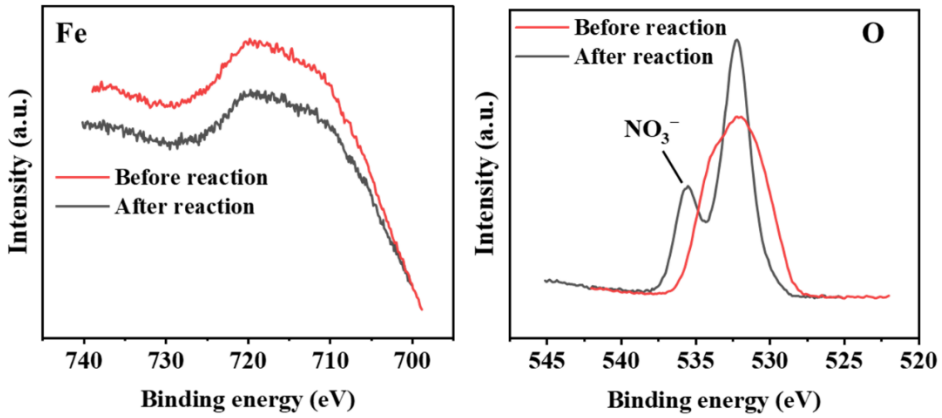

Supplementary Figure 26. XPS patterns of HS-LFP electrode before and after long-term stability test.

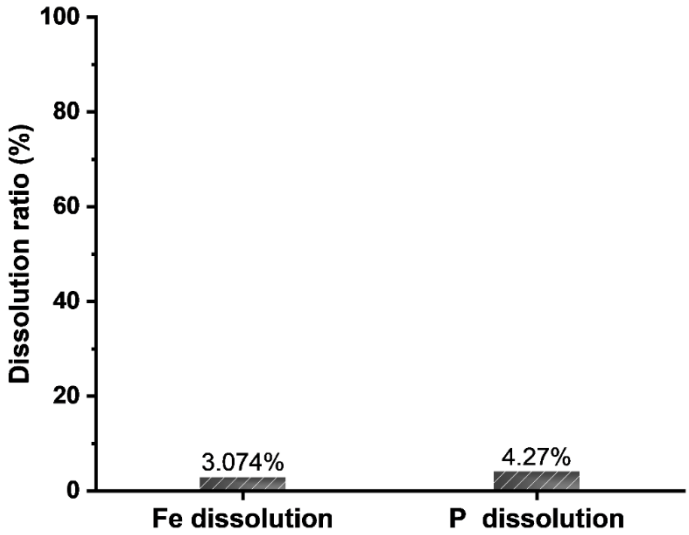

Supplementary Figure 27. Quantitative ICP results of Fe and P dissolution after the long-term stability test.

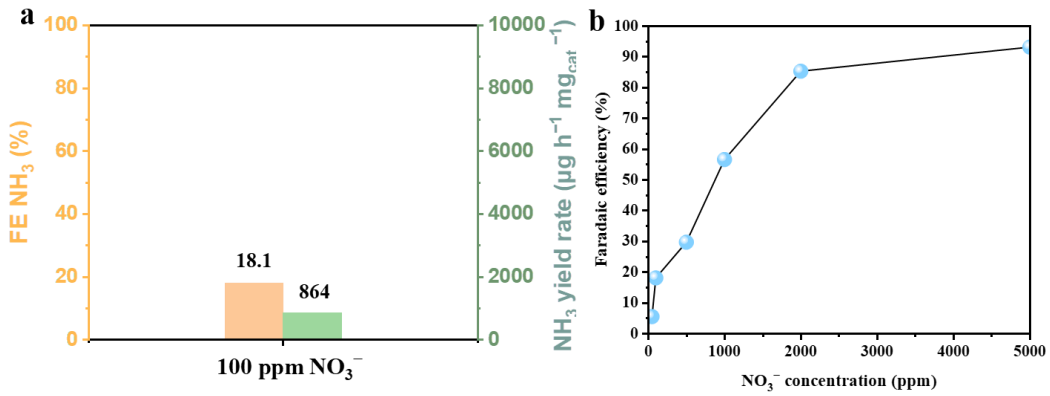

Supplementary Figure 28. (a) NH_3 Faradaic efficiency and NH_3 yield rate of HS-LFP at a low nitrate concentration of 100 ppm NO_3^-. (b) Dependence of NH_3 Faradaic efficiency on NO_3^- concentration.

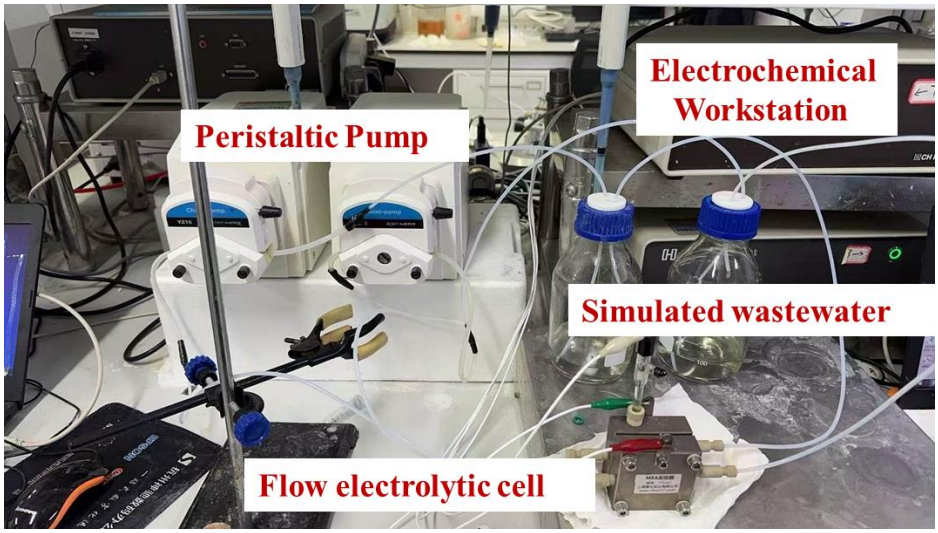

Supplementary Figure 29. The photograph of the flow-cell system. Photographs in Supplementary Figure 29 were taken by the authors.

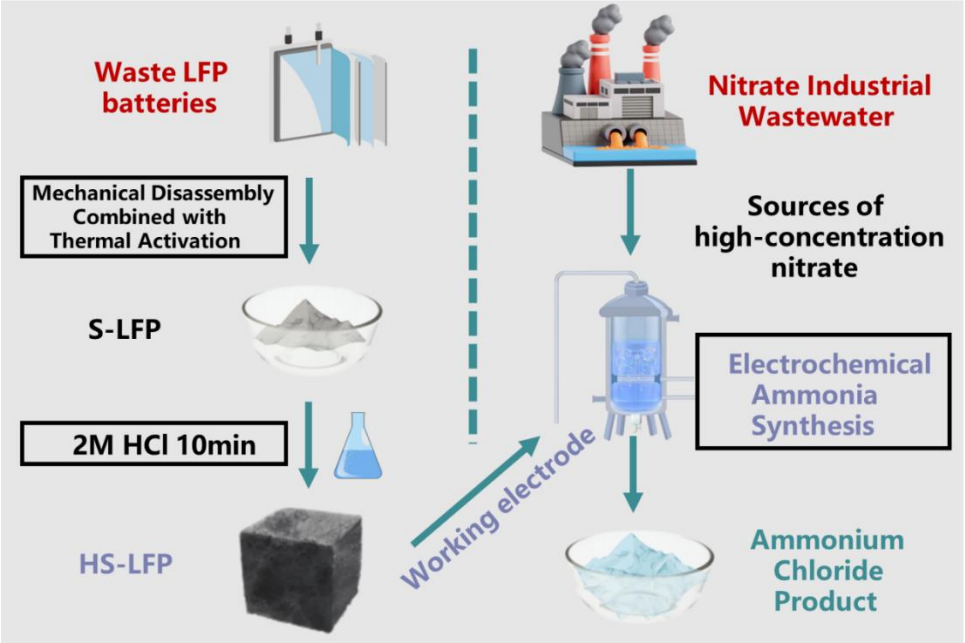

Supplementary Figure 30. Full-scale preparation and application workflow of HS-LFP catalyst.

Supplementary Table 1. Comparison of NO_3RR performances for NH_3 production between our prepared catalyst and the reported catalysts

Materials	Electrolyte	FE(NH_3) (%)	Applied potential (V vs. RHE)	NH_3 yield rate ($\mu g\ h^{-1}\ mg_{cat}^{-1}$)	Reference
HS-LFP	1 M KOH and 0.1 M KNO_3	61.1	-0.6	20247	This work
HS-LFP	1 M KOH and 0.1 M KNO_3	98.28	-0.4	14232	This work
Fe/Cu-HNG	1 M KOH and 0.1 M KNO_3	92.5	-0.5	4403	[4]
Pd-CuO	1 M KOH and 0.1 M KNO_3	90.0	-0.5	15708	[5]
Cu_3N/GDY	1 M KOH and 0.1 M KNO_3	98.1	-0.9	35280	[6]
CuCoSP	0.1 M KOH and 0.1 M KNO_3	90.6	-0.175	19890	[7]
MP-Cu	1 M KOH and 0.05 M KNO_3	99.8	-0.3	9230	[8]

Fe-ppy SACs	0.1 M KOH and 0.1 M KNO_3	~100	-0.7	11400	[9]
CoP NAs/CFC	1 M KOH and 1 M NO_3	~100	-0.3	9700	[10]
$Cu/Co_{0.85}Se_{VSe}$	0.1 M KOH and 0.01 M KNO_3	93.5	-0.6	2360	[11]
Fe-N/P-C	0.1 M KOH and 0.1 M KNO_3	90.28	-0.4	5850	[12]
Co-CNP	0.02 M Na_2SO_4 and 0.071 M NO_3-N	91.8	-0.69	68	[13]
FeCo/C-0.5	1 M KOH and 0.1 M KNO_3	85.35	-0.58	16204	[14]
$Ru_1/Co(OH)_2$	0.1 M KOH and 0.071 M NO_3-N	97.00	-0.33	4200	[15]
Fe SAC	0.1 M K_2SO_4 and 0.5 M KNO_3	75.00	-0.66	2400	[16]
$ZnCo_2O_4$	0.1 M KOH and 0.1 M NO_3^-	95.40	-0.40	2100	[17]

REFERENCES

1. Li, J.; Li, M.; An, N.; et al. Boosted ammonium production by single cobalt atom catalysts with high Faradic efficiencies. *Proc. Natl. Acad. Sci. U.S.A.* **2022**, 119, e2123450119 DOI: 10.1073/pnas.2123450119.
2. Zhu, J.; Cai, L.; Tu, Y.; et al. Emerging ruthenium single-atom catalysts for the electrocatalytic hydrogen evolution reaction. *J. Mater. Chem. A* **2022**, 10, 15370-15389 DOI: 10.1039/D2TA03860A.
3. Zhang, W.-D.; Dong, H.; Zhou, L.; et al. Fe single-atom catalysts with pre-organized coordination structure for efficient electrochemical nitrate reduction to ammonia. *Appl. Catal. B-Environ.* **2022**, 317, 121750 DOI: 10.1016/j.apcatb.2022.121750.

4. Zhang, S.; Wu, J.; Zheng, M.; et al. Fe/Cu diatomic catalysts for electrochemical nitrate reduction to ammonia. *Nat Commun* **2023**, 14, 3634 DOI: 10.1038/s41467-023-39366-9.

5. Liu, Y.; Zhuang, Z.; Liu, Y.; et al. Shear-Strained Pd Single-Atom Electrocatalysts for Nitrate Reduction to Ammonia. *Angew Chem Int Ed* **2024**, e202411396 DOI: 10.1002/anie.202411396.

6. Zhang, Z.; Feng, X.; Zhang, Z.; et al. Graphdiyne Enabled Nitrogen Vacancy Formation in Copper Nitride for Efficient Ammonia Synthesis. *J. Am. Chem. Soc.* **2024**, 146, 14898-14904 DOI: 10.1021/jacs.4c04985.

7. He, W.; Zhang, J.; Dieckhöfer, S.; et al. Splicing the active phases of copper/cobalt-based catalysts achieves high-rate tandem electroreduction of nitrate to ammonia. *Nat Commun* **2022**, 13, 1129 DOI: 10.1038/s41467-022-28728-4.

8. Wen, W.; Yan, P.; Sun, W.; et al. Metastable Phase Cu with Optimized Local Electronic State for Efficient Electrocatalytic Production of Ammonia from Nitrate. *Adv Funct Materials* **2023**, 33, 2212236 DOI: 10.1002/adfm.202212236.

9. Li, P.; Jin, Z.; Fang, Z.; et al. A single-site iron catalyst with preoccupied active centers that achieves selective ammonia electrosynthesis from nitrate. *Energy Environ. Sci.* **2021**, 14, 3522-3531 DOI: 10.1039/D1EE00545F.

10. Ye, S.; Chen, Z.; Zhang, G.; et al. Elucidating the activity, mechanism and application of selective electrosynthesis of ammonia from nitrate on cobalt phosphide. *Energy Environ. Sci.* **2022**, 15, 760-770 DOI: 10.1039/D1EE03097C.

11. Gu, Z.; Zhang, Y.; Wei, X.; et al. Intermediates Regulation via Electron-Deficient Cu Sites for Selective Nitrate-to-Ammonia Electroreduction. *Advanced Materials* **2023**, 35, 2303107 DOI: 10.1002/adma.202303107.

12. Xu, J.; Zhang, S.; Liu, H.; et al. Breaking Local Charge Symmetry of Iron Single Atoms for Efficient Electrocatalytic Nitrate Reduction to Ammonia. *Angew Chem Int Ed* **2023**, 62, e202308044 DOI: 10.1002/anie.202308044.

13. Li, J.; Li, M.; An, N.; et al. Boosted ammonium production by single cobalt atom catalysts with high Faradic efficiencies. *Proc. Natl. Acad. Sci. U.S.A.* **2022**, 119, e2123450119 DOI: 10.1073/pnas.2123450119.

14. Eziz, A.; Abulizi, A.; Liang, C.; et al. Doping-Engineered Fe-Co Tandem Sites Balance Hydrogen and Nitrite Intermediates for Efficient Nitrate to Ammonia Conversion at Low Potential. *Small* n/a, e73610 DOI: 10.1002/smll.73610.

15. Zhang, J.; Liu, Y.; Zhang, J.; et al. Engineering Single-Atomic Ru Sites on Cobalt Hydroxide Boosts Atomic Hydrogen Generation for Efficient Nitrate Electroreduction to Ammonia. *Renewables* **2025**, 3, 99-110 DOI: 10.31635/renewables.025.202500086.

16. Wu, Z.-Y.; Karamad, M.; Yong, X.; et al. Electrochemical ammonia synthesis via nitrate reduction on Fe single atom catalyst. *Nat Commun* **2021**, 12, 2870 DOI: 10.1038/s41467-021-23115-x.

17. Huang, P.; Fan, T.; Ma, X.; et al. 3D Flower-Like Zinc Cobaltite for Electrocatalytic Reduction of Nitrate to Ammonia under Ambient Conditions. *ChemSusChem* **2022**, 15, e202102049 DOI: 10.1002/cssc.202102049.